

Laser-induced spectral diffusion and excited-state mixing of silicon T centres

Camille Bowness^{12,*}, Simon A. Meynell^{12,*}, Michael Dobinson¹², Chloe Clear², Kais Jooya¹², Nicholas Brunelle¹², Mehdi Keshavarz¹², Katarina Boos³, Melanie Gascoine¹², Shahrzad Taherizadegan⁴⁵, Christoph Simon⁴⁵, Mike L. W. Thewalt¹, Stephanie Simmons¹², and Daniel B. Higginbottom¹²

¹*Simon Fraser University, Department of Physics, Burnaby, British Columbia, Canada*

²*Photonic Inc., Coquitlam, British Columbia, Canada*

³*Walter Schottky Institut, Department of Electrical and Computer Engineering and MCQST, Technische Universität München, 85748 Garching, Germany*

⁴*University of Calgary, Department of Physics and Astronomy, Calgary, Alberta, Canada and*

⁵*Institute for Quantum Science and Technology, University of Calgary, Calgary, Alberta, Canada*

(Dated: April 15, 2025)

To find practical application as photon sources for entangled optical resource states or as spin-photon interfaces in entangled networks, semiconductor emitters must produce indistinguishable photons with high efficiency and spectral stability. Nanophotonic cavity integration increases efficiency and bandwidth, but it also introduces environmental charge instability and spectral diffusion. Among various candidates, silicon colour centres have emerged as compelling platforms for integrated-emitter quantum technologies. Here we investigate the dynamics of spectral wandering in nanophotonics-coupled, individual silicon T centres using spectral correlation measurements. We observe that spectral fluctuations are driven predominantly by the near-infrared excitation laser, consistent with a power-dependent Ornstein-Uhlenbeck process, and show that the spectrum is stable for up to 1.5 ms in the dark. We demonstrate a $35\times$ narrowing of the emitter linewidth to 110 MHz using a resonance-check scheme and discuss the advantage for pairwise entanglement rates and optical resource state generators. Finally, we report laser-induced spin-mixing in the excited state and discuss potential mechanisms common to both phenomena. These effects must be considered in calibrating T centre devices for high-performance entanglement generation.

Semiconductor point defects are a versatile platform for quantum technologies [1], they can function as single-photon sources for quantum communication and as resource state generators for optical quantum computers [2]. If the emitter couples single photons to a local spin qubit, then it may also function as a spin-photon interface (SPI) with applications including quantum repeater networks [3, 4] and hybrid spin-photon quantum computing [5–7]. Semiconductor emitters may be integrated directly into nanophotonic optical resonators to enhance their emission rate and coherence through the Purcell effect [8, 9]. In turn, these optical resonators can be connected by photonic integrated circuits to prepare large entangled states on-chip [10]. However, integration also exposes the emitter to material interfaces and crystal damage that produce charge noise and cause the emission frequency to fluctuate in time [11, 12]. Such spectral diffusion (SD, also called spectral wandering) is a critical challenge for practical quantum technologies.

Recently, silicon colour centres have emerged as an intriguing category of emitters harnessing the advanced material and nanofabrication capabilities of silicon [13–18]. The silicon T centre, for example, is the focus of ongoing commercial efforts to build a spin-photon quantum computer [5, 19]. Silicon combines global microelectronics and nanophotonics foundry capabilities with extremely high chemical and isotopic purities [20]. Owing to the mass homogeneity, strain-free environment,

and high-quality lattice of their “semiconductor vacuum” host, the optical transitions of silicon colour centres in bulk ^{28}Si crystals can have remarkably low inhomogeneous broadening and spectral diffusion. Popular silicon colour centres including C and T have demonstrated inhomogeneous linewidths below 60 MHz and the G centre can be nearly lifetime-limited [21, 22]. However, spectral diffusion has proven to be significant in the first generation of silicon colour centre devices [13, 18, 19, 23] and increasing the spectral stability closer to their performance in bulk is a critical challenge.

Interference-based entanglement protocols require spectrally matched, stable emitters [24, 25]. Resonant excitation using a shared, narrow-linewidth laser acts as a frequency filter, selecting only emitters that are spectrally aligned. However, spectral diffusion reduces the probability of such alignment by a factor of $\approx \eta_{\text{SD}}^2$, where $\eta_{\text{SD}} = \Gamma_{\text{hom}}/\Gamma_{\text{SD}}$ is the ratio of the SD and homogeneous linewidths. For example, SD decreases the entanglement rate between remote T centre devices by three orders of magnitude in Ref. [19]. Techniques for reducing or mitigating spectral diffusion have been widely explored for other semiconductor emitters. Resonance-check (RC) techniques can confirm both the charge state of diamond colour centres (e.g. NV, SiV and SnV) and mutual resonance between remote emitters [26, 27]. In wide-bandgap semiconductors, spectral diffusion is relatively slow (\sim s) [28, 29], and hundreds of entanglement attempts may follow a single RC [30]. In contrast, resonantly driven silicon colour centres exhibit emission correlations typical of short SD timescales of 5–10 μs [13, 19].

* These authors contributed equally.

In this paper, we investigate spectral diffusion processes in single, cavity-coupled silicon T centres, shown schematically in Fig. 1. We show through spectrally-resolved two-photon correlations in the device luminescence that spectral diffusion of the TX_0 transition is driven predominantly by the interaction of the NIR laser and the material. We show that resonance checks can dramatically narrow the effective linewidth of T centres in devices, and that they remain effective for up to ~ 1.5 ms of wait-time in the dark. We explore the conditions under which they can achieve a practical speedup for entangled state generation. Finally, we investigate the effect of NIR laser on the spin of the optically-excited bound-exciton state TX_0 . Together, these results illustrate the mechanism of laser-induced spectral diffusion and demonstrate a promising approach to mitigate spectral diffusion in T centre devices. These results have immediate relevance for near-term T centre quantum processors and network demonstrations.

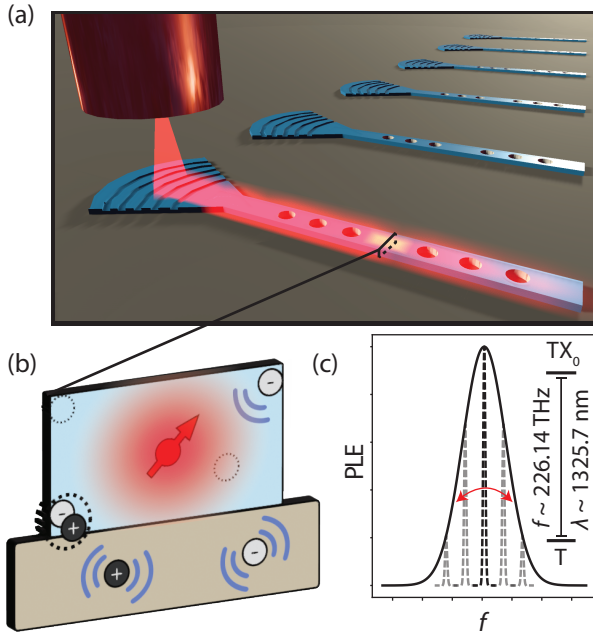


FIG. 1. Spectral diffusion in integrated colour centre devices. (a) A 1D silicon photonic crystal cavity is addressed by a resonant laser through an off-chip optical fibre and a grating coupler. (b) Cross section showing an integrated T centre at the device centre. The laser resonates in the single-mode cavity (red). Charge traps at surfaces, interfaces, impurities, and vacancies within the silicon device layer and oxide insulator generate electric fields that perturb the colour centre emission frequency. (c) An illustration of spectral diffusion. The T centre emission frequency fluctuates as the charge environment is reconfigured.

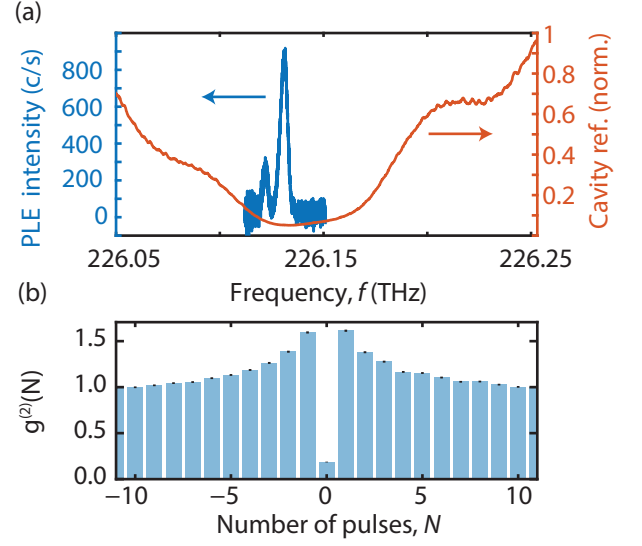


FIG. 2. A representative integrated T centre device (T Centre II). (a) The photoluminescence excitation (PLE) spectrum at zero magnetic field (blue), and the cavity spectrum measured in reflection (orange). (b) Correlation measurements of the centre luminescence under pulsed resonant excitation exhibit a high degree of antibunching with $g^{(2)}(0) = 0.186(4) \ll 1$, confirming the emission is dominated by a single centre. $g^{(2)}(N)$ shows a positive correlation at low pulse separation number N , a characteristic signature of spectral diffusion [31].

I. SPECTRAL DIFFUSION OF DEVICE-INTEGRATED T CENTRES

We characterize the spectral diffusion dynamics of integrated, single T centres with and without near-infrared (NIR) excitation. The T centre is a silicon colour centre combining telecommunications-band optical emission, a ground-state electron spin qubit, and an intrinsic register of 1–3 nuclear spin qubits depending on isotopic composition. Since it was first proposed for quantum technologies in 2020 [22], it has been integrated with silicon nanophotonics [13, 32], Purcell-enhanced in nanocavities [14, 18, 19, 33, 34], and embedded in p-i-n diode devices for electrical control [34, 35]. Moreover, these devices exhibit strong qubit performance: one- and two-qubit gates have been realized using the electron and hydrogen nuclear spins; nuclear coherence times exceeding 200 ms have been demonstrated; and indistinguishable emission has been observed between devices in separate cryostats [19]. In high purity, isotopically-enriched bulk ^{28}Si samples the T centre’s inhomogeneous linewidth (including static spatial inhomogeneity and SD) is as low as 33 MHz [22], just 15 times the lifetime-limit of Purcell-enhanced T centres in devices [19]. However, the typical SD linewidth of integrated T centres observed to date is much larger, 0.4–4 GHz [13, 14, 18, 36].

The centres in our study are integrated in 1D silicon photonic crystal cavities on a silicon-on-insulator chip

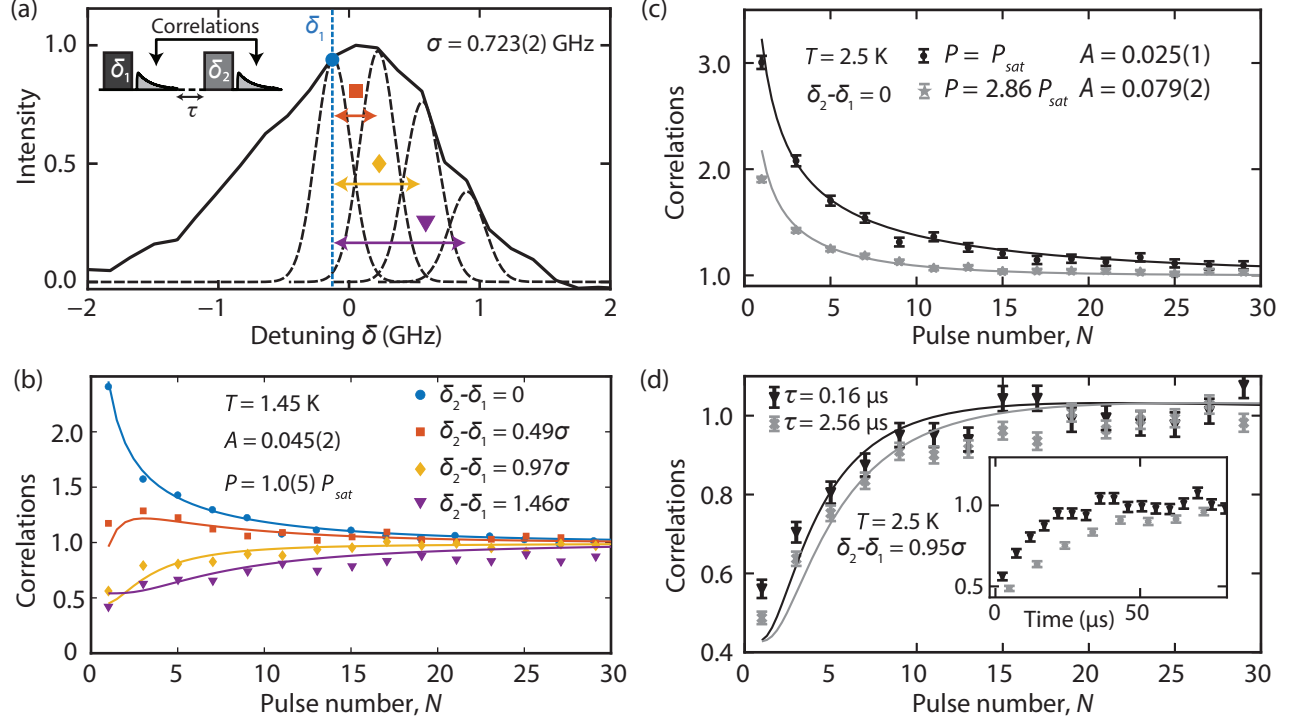


FIG. 3. Two-colour correlation measurement. (a) Laser detunings $\delta_{1,2}$ from the centre of the inhomogeneous line (solid) and modelled homogeneous lines (dashed). The vertical blue line indicates δ_1 . (Inset) Pulse sequence showing consecutive excitation pulses at detunings $\delta_{1,2}$. Correlations are calculated between photons emitted in detection windows indicated by the grey luminescence transients. (b) Correlations between frequencies $\delta_{1,2}$ as a function of the number of intermediate pulses. Solid lines display a joint single-parameter (A) fit to an O-U model of spectral diffusion. (c) Power dependence of the two colour correlation for two different powers. The correlation amplitude reduces with higher power. (d) Dark-time dependence of the two-colour correlation. The curves show closer agreement when plotted as a function of pulse number compared to when they are plotted as a function of time (inset).

and resonantly excited to the bound-exciton ground state TX_0 . We report results from two devices, T Centre I and II, with moderate cavity quality factors $Q_I = 880(40)$ and $Q_{II} = 1,743(2)$ such that the cavities can be excited on- or off-resonance from the T centres. The devices are operated at either 0.4 K or 1.45 K–2.5 K in one of two cryostats, and addressed by cryogenic optical fibre arrays (see Methods for more details). Figure 2 shows the photoluminescence excitation (PLE) spectrum and $g^{(2)}$ of T Centre II. Details of the devices reported in this study are provided in the Supplementary Material (SM) Sec. 1 [37].

A. Two-colour correlation

We measure spectral dynamics using frequency-resolved photon correlation measurements. For this experiment, we choose a device (T Centre I) with a PLE full width at half maximum linewidth $\Gamma = 1.694(5)$ GHz (standard deviation $\sigma = 0.723(2)$ GHz). Spectral hole-burning measurements of the homogeneous linewidth, Γ_{hom} (see SM [37]), confirm a temporal inhomogeneous

broadening factor of $1/\eta_{SD} = \Gamma/\Gamma_{hom} \geq 52(7)$. With the sample at 1.45 K, we detune two sub-MHz linewidth excitation lasers from the PLE peak by frequencies δ_1 and δ_2 . We measure correlations between photons emitted in detection bins corresponding to each of the two excitation frequencies, and separated by inter-pulse delay $\tau = 160$ ns, using the pulse sequence in Fig. 3(a). Each pulse is 900 ns in duration and followed by a 1,375 ns collection window.

We fix δ_1 at the centre frequency and vary δ_2 across four values shown in Fig. 3(a). When the detuning difference $\delta_2 - \delta_1 = 0$ (*i.e.*, single laser PLE), detections in consecutive windows are positively correlated, as observed in the $g^{(2)}$ measurement. The emitter has a spectral diffusion time larger than the pulse sequence length, and if it is resonant for the first pulse it is more likely to be resonant for the second. On the other hand, if the two lasers are separated by 0.97σ , emission into consecutive time bins is anticorrelated, since a finite time is required for the emitter to wander from frequency δ_1 to δ_2 . We model the spectral diffusion as an Ornstein-Uhlenbeck (O-U) process (solid lines in Fig. 3(b)–(d)), parametrized solely by the SD rate during the excitation pulse, α , and

the ratio of background counts to total counts, β [38]. We use a closed form expression for the correlations and connect it to a discrete charge microscopic model (details in SM [37]). We obtain β by comparing the uncorrelated PLE count rate as a function of frequency to our background rate. Finally, we extract the SD rate α by jointly fitting the correlation data taken at 1.45 K across multiple detuning values, $\delta_2 - \delta_1 = 0, 0.49\sigma, 0.97\sigma, 1.46\sigma$ and extract a per-pulse rate of $A = \int_{\text{pulse}} \alpha dt = 0.045(2)$. We repeat the measurements at 2.5 K and find a similarly good match to the model (see SM [37]).

To test the SD mechanism, we next investigate how the correlation measurements depend on laser power (Fig. 3(c)). Here, we keep $\delta_2 - \delta_1 = 0$ and change between two powers, P_{sat} and $2.86P_{\text{sat}}$ where P_{sat} is the calibrated saturation power. We observe that the correlation amplitude drops with increasing power, consistent with an increase in SD rate. Hole-burning measurements (see SM [37]) verify that the homogeneous linewidth is stable over this power range. The O-U model (solid lines) agrees well with the ratio of fitted charge reconfiguration rates, $A(P_{\text{sat}})/A(2.86P_{\text{sat}}) = 0.025(1)/0.079(2) = 0.32(2)$, matching the ratio of powers (0.35), which suggests that the fraction of charges reconfigured per pulse scales with the incident intensity. We further observe that adding a near-resonant laser has the same effect as increasing the resonant power (see SM [37]), indicating that the effect is consistent with a broadband interaction with the host material.

Finally, we increase the delay τ between the two-colour pulses from $\tau = 160$ ns to 2,560 ns. The resulting correlation curves, shown in Fig. 3(d), differ when plotted as a function of absolute time but show close agreement when the data are plotted as a function of pulse number, indicating that spectral wandering is negligible during the dark inter-pulse time. Fitting each dataset with a fixed value of β , we extract $A(\tau = 160 \text{ ns}) = 0.024(2)/\text{pulse}$ and $A(\tau = 2,560 \text{ ns}) = 0.019(2)/\text{pulse}$. That A scales with pulse number and power, rather than time, indicates that the diffusion is driven by the energy delivered by each excitation pulse. This is consistent with the findings of van de Stolpe *et al.*, which identified laser-induced spectral diffusion in emitters in silicon carbide [39], and analogous behaviour observed in SnV centres [40]. The slow spectral diffusion of the T centre in the absence of optical excitation suggests a strategy for multi-emitter alignment: after a successful resonance check, waiting in the dark may preserve the emitter's spectral position long enough to synchronize multiple T centres.

B. Resonance-check spectroscopy

We investigate a RC scheme [26, 39] as an initialization step for preceding resource state generation or bipartite entanglement attempts. We choose a second device on the same chip (T centre II, see SM [37]) at temperature $T = 0.4$ K and apply a series of pulses detuned by δ_1 to

prepare the T centre at a target optical frequency. Following a photon detection that heralds resonance with the ‘check’ laser, we proceed with the target application. In this case, we perform PLE measurements conditioned on the resonance check by sending a low-power ‘probe’ pulse at frequency δ_2 after a delay τ , as illustrated in Fig. 4(a). If SD between the check and probe pulses is negligible, the RC-conditioned PLE linewidth measured by the probe pulse should be narrower than the raw PLE spectrum. Indeed, at the lowest-power setting, check (probe) power $P_{\delta_1} = 0.016P_{\text{sat}}$ ($P_{\delta_2} = 0.008P_{\text{sat}}$), we observe a linewidth of 110(10) MHz, $35\times$ narrower than the raw PLE linewidth as shown in Fig. 4(b). Following the resonance check, the photon-detection probability increases by $6\times$.

To test for spectral diffusion in the absence of excitation, we vary the dark interval τ and monitor the RC linewidth. To improve count rates, we increase the powers for the check and probe lasers to $P_{\delta_1} = 0.19P_{\text{sat}}$ and $P_{\delta_2} = 0.11P_{\text{sat}}$. At these powers, the $\tau = 0$ RC-conditioned linewidth is 1.2(1) GHz and shows no significant broadening out to $\tau = 1.5$ ms (Figure 4(c)). However we observe a small increase in linewidth at $\tau \gtrsim 2.5$ ms (see the SM [37]). Independent T centre devices can therefore be prepared by resonance checks, and remain stable for milliseconds—sufficient time to prepare additional devices.

RC schemes offer considerable advantages in scaling SPIs to generate large optical resource states [41–43] by preparing N qubits with identical optical frequencies. Interference-based remote entanglement schemes such as the Barrett-Kok protocol [24], demonstrated with T centre devices in Ref. [19], require $N = 2$ spectrally indistinguishable qubits, but optical resource state generator schemes can require many simultaneously resonant emitters. In the example scheme proposed by Wein *et al.*, 12 SPIs are first entangled by pairwise operations, before all $N = 12$ are required to emit simultaneously at the target frequency [44].

We derive the expected number of attempts T required to prepare N qubits by RC

$$\mathbb{E}[T] = \sum_{j=1}^N (-1)^{j+1} \binom{N}{j} \frac{1}{1 - (1 - \eta_{\text{SD}}\eta_{\text{det}})^j}, \quad (1)$$

where η_{det} is the detection efficiency. If the effective linewidth ratio under the RC scheme is given by η'_{SD} , the resulting speedup in preparing N qubits is

$$\text{Speedup} = \frac{(\eta'_{\text{SD}}/\eta_{\text{SD}})^N}{1 + \mathbb{E}[T]}, \quad (2)$$

which is shown as a function of N and η_{det} in Fig. 4(d). Even for small N , the improvement can be many orders of magnitude. Moreover, the RC scheme also offers benefits in protocols that involve long spin control sequences or sequential photon generation, where each step depends on the success of prior emission events [45].

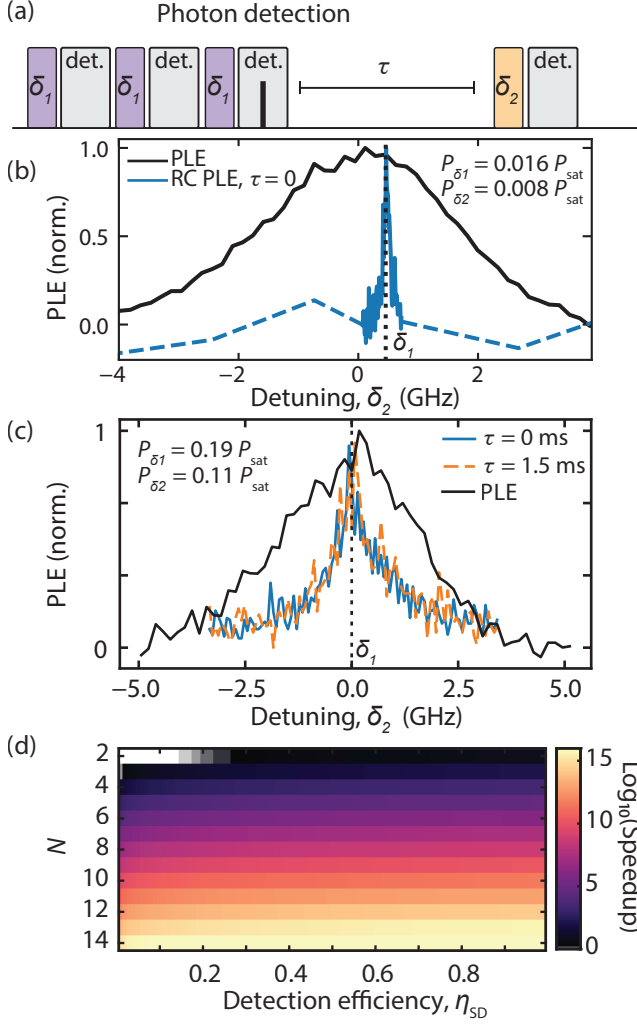


FIG. 4. Resonance check (RC) PLE scheme. (a) The experimental pulse sequence. We excite at check frequency δ_1 until a photon is detected, which triggers a probe pulse at frequency δ_2 after delay τ . (b) RC PLE compared to regular PLE showing the linewidth narrowing to $\Gamma = 110(10)$ MHz. (c) RC PLE with dark wait time, τ . We probe broadening in the absence of laser excitation as a function of wait time and observe no significant broadening out to 1.5 ms. (d) N -qubit entangled state preparation with parallel RCs. The speedup, defined as τ^*/τ_{RC} , where τ_{RC} is the time required to obtain N resonant photons from N independent T centres prepared with RC PLE and τ^* is the time it takes to obtain N resonant photons from N independent T centres prepared conventionally. White indicates the region where no speedup is expected.

II. LASER-INDUCED EXCITED STATE SPIN MIXING

We observe a second laser-driven effect causing TX_0 spin mixing, which disrupts the cyclicity of otherwise spin-conserving transitions and reduces the fidelity of repeated spin-photon entanglement cycles. We apply a magnetic field $B = 755$ mT along $[110]$ to T centre II

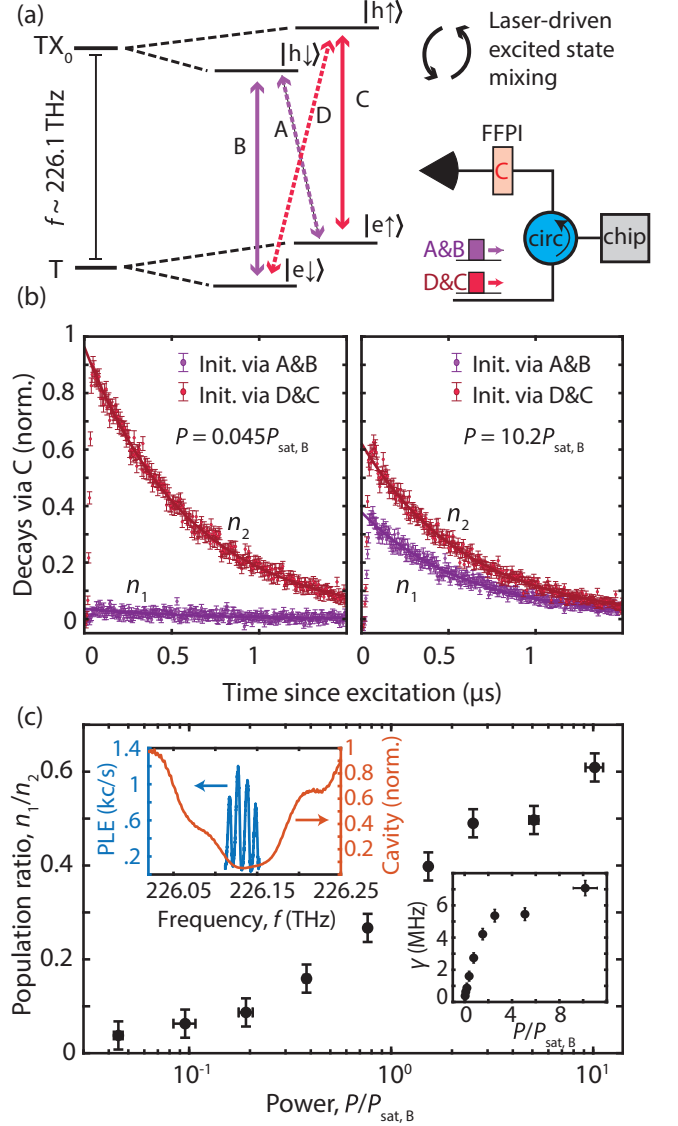


FIG. 5. TX_0 spin populations as mixed by laser power. (a) The level diagram of T centre II under an applied field and experiment schematic. (b) Time-resolved decay measurements showing the populations converging at higher excitation powers, indicating increased spin mixing. Powers are quoted in the at-field saturation power, $P_{sat,B}$. (c) Population ratio n_1/n_2 as a function of excitation power. The insets show the at-field PLE spectrum for this T centre (top) and the extracted mixing rate γ versus power (bottom).

with a superconducting Helmholtz coil pair to lift the spin degeneracy, as shown in Figure 5(a), and operate at $T = 0.4$ K to reduce post-pulse thermal effects. We prepare either of the two TX_0 states $|h\uparrow\rangle$ (red) and $|h\downarrow\rangle$ (purple) by spin-selective excitation and align a fibre Fabry-Pérot interferometer to filter spin-selective luminescence from the C transition, which allows us to measure the population in $|h\uparrow\rangle$.

Figure 5(b) shows the $|h\uparrow\rangle$ population as a function

of time for both spin preparation schemes, where n_1 and n_2 are the population following preparation of $|h \downarrow\rangle$ and $|h \uparrow\rangle$ respectively. The left panel shows relative populations for low-power preparation ($P = 0.045P_{\text{sat, B}}$), while the right shows high-power preparation ($P = 10.2P_{\text{sat, B}}$), where $P_{\text{sat, B}}$ is the at-field saturation power. Single exponential fits match the decay with no measurable indication of post-pulse thermalization.

The ratio n_1/n_2 corresponds to the degree of spin mixing (given equal mixing rates as shown in SM [37]) and increases from 0 (no mixing) to ≈ 0.6 with increasing excitation power as shown in Fig. 5(c). Assuming perfect spin-state initialization and uniform excitation during the pulse, we define an effective mixing rate

$$\gamma = \frac{1}{2T} \ln \left(\frac{n_2 + n_1}{n_2 - n_1} \right), \quad (3)$$

plotted in the inset of Fig. 5(c). Finally, we find that excited-state spin mixing is not a resonant effect. When the experiment is repeated at low resonant powers with additional high-power off-resonant light, we observe similar levels of mixing (see SM [37]).

This mixing effect reduces the optical cyclicity (the average number of optical cycles before the spin state flips) of T centre devices below the dipole branching ratio limit [46], with consequences for quantum non-demolition readout by resonant excitation and for remote entanglement schemes requiring cyclic transitions [24].

III. DISCUSSION

Our results establish the significance of laser-induced effects for silicon colour centre emitters and SPIs. We find that the spectral diffusion of T centres in nanophotonic devices is primarily induced by the NIR excitation laser and, using a resonance-check scheme, we achieve a $\times 35$ reduction in effective linewidth to 110(10) MHz. We expect that the RC linewidth can be further reduced towards the homogeneous limit (51 MHz, see SM [37]) by optimizing the check/probe pulses. We find that the RC linewidth remains stable for up to ~ 1.5 ms, long enough for practical advantage. Along with concurrent work in Ref. [47], this is the first demonstration of a functional RC scheme for silicon colour centres to our knowledge.

Effective RCs enhance the feasibility of interference-based silicon colour centre quantum technologies, increasing emission efficiencies for resource state generation and other protocols requiring spectrally matched emitters or photons. Under a wide range of conditions, RCs can improve the performance of even pairwise ($N = 2$) entanglement schemes [48]. We anticipate that the scheme introduced here can be applied to improve the entanglement rate of prototype T centre repeaters, network hubs, and spin-photon processors [5, 19].

Finally, we observe laser-induced spin mixing in the optically-excited bound-exciton state TX_0 . We suggest that these two laser-induced effects have the same root

cause. A broad, low intensity band, likely a superposition of donor-acceptor-pair bands, is common to radiation-damaged silicon photoluminescence and underlies the sharp emitter lines of T and other silicon colour centres. This band may be due to donor- and acceptor-like damage centres. We observe that the NIR excitation laser, detuned from the T centre or any other sharp lines, drives luminescence from this broad band. This indicates that the laser is weakly photoneutralizing these ionized defects so they can recombine and luminesce. Such laser-driven charge fluctuations would cause T centre spectral wandering, and could also couple to the TX_0 hole state to induce spin-state mixing.

Photo-induced spectral diffusion has been extensively studied in quantum dots (QDs) [49–51]. These studies identify surface traps and charge traps in surrounding oxide layers as major contributors to spectral diffusion [52, 53] and the same mechanisms may be present at the interfaces and oxide layers of our devices. Efforts to passivate QD surfaces have led to significant improvements in spectral stability [53], and the same engineering approaches may, in the longer term, reduce the silicon colour centre spectral diffusion closer to their performance in bulk, and perhaps make resonance checks redundant. These results are critical for understanding and mitigating laser-driven processes that limit the fidelity and success rate of multi-qubit entanglement sequences with silicon T centres and should be relevant to a broad class of emerging devices, as well as electronically similar silicon colour centres [54].

ACKNOWLEDGMENTS

This work was supported by the Natural Sciences and Engineering Research Council of Canada (NSERC) through Discovery Grants held by D.B.H., S.S., M.L.W.T. and C.S. and the ARAQNE Quantum Alliance Consortium, the New Frontiers in Research Fund (NFRF), the Canada Research Chairs program (CRC), the Canada Foundation for Innovation (CFI), the B.C. Knowledge Development Fund (BCKDF), and the Canadian Institute for Advanced Research (CIFAR) Quantum Information Science program. S.A.M. acknowledges support from NSERC Postdoctoral Fellowship 571590123. S.T. and C.S. acknowledge support by the National Research Council through its High-Throughput Secure Networks (HTSN) Challenge Program.

The chip was provided by our industry partner Photonic Inc. We are grateful to Amin Khorshidahmad, Francis Afzal, Iain MacGilp, and Mohsen Akhlaghi and the entire Integrated Photonics team for their support of this project. We would also like to thank Evan MacQuarrie and Ata Ulhaq for their thorough review of the manuscript and helpful perspective throughout the project.

During the preparation of this manuscript, we became aware of related work Ref. [47].

Appendix A: Methods

1. Sample

T centres are generated in a float-zone p-type SOI chip using a multi-stage implant and anneal process following MacQuarrie *et al.* [36]. Photonic devices are patterned by e-beam lithography and etched into the chip. We use quadratically tapered L0 nanobeam cavities ([55]) with the cavity-axis along [110] to enhance our T centre emission rate through the Purcell effect. We find quality factors of $Q = 600\text{--}2,000$. Single-mode waveguides couple the nanobeam cavities to on-chip diffraction grating couplers with 6 THz bandwidths centred between 223.7 THz–228.9 THz that couple light into and out of the chip via optical fibres.

2. Apparatus

For the two-colour spectroscopy, two fibre-coupled, tuneable, continuous-wave lasers (Toptica CTL) are pulsed independently and combined. Each laser is frequency-locked to a Bristol wavemeter. Pulsing is achieved using a booster optical amplifier (BOA) and an electro-optical modulator (EOM). We adjust the power of each laser using a combination of manual variable optical attenuators (VOA) and electrically variable optical attenuators (EVOA). The two lasers are combined using a fibre-coupled 50/50 splitter, then a circulator connects them to polarization maintaining fibres which feed into a custom cryogenic fibre array to deliver light to the sample held at temperatures between 1.45 K–2.5 K in an ICE Oxford He flow cryostat. Reflected laser light and T centre emission are collected through the same fibre path and routed to superconducting nanowire single photon detectors (SNSPDs) housed in a separate cryostat (IDQ 281).

The configuration for the resonance-check measurements is the same as for the two-colour correlation measurements with two additional components: An AOM is placed in the excitation path between the EOM and the circulator to improve the pulse extinction ratio, and an AOM is inserted in the collection path between the circulator and the SNSPDs to prevent detector saturation during the excitation pulse. In this experiment, the samples are housed in a Bluefors LD400 dilution refrigerator, with the devices thermally anchored to a mixing plate held at 0.4 K.

The configuration for the laser-induced hole-spin mixing is the same as the resonance-check measurements without the AOM in the excitation path. A fibre-coupled, temperature-tuneable Fabry-Perot interferometer with a bandwidth of 0.985 GHz and free spectral range of 102.4 GHz (LUNA Innovations) is added in the collection path. Two optical isolators are placed before and after the interferometer to suppress reflections.

**SUPPLEMENTAL MATERIAL FOR: “LASER-INDUCED SPECTRAL DIFFUSION AND
EXCITED-STATE MIXING OF SILICON T CENTRES”**

Appendix SI: Summary of measured devices

Table S1 summarizes the key experimental parameters and figures of merit for the two T centre devices (T Centre I and II) presented in the manuscript and a third device (T Centre III) included here for additional verification. T centre I was measured in an ICE Oxford He-flow cryostat at 1.5 and 2.5 K, while T centres II and III were measured in a Bluefors LD400 dilution refrigerator.

	T centre I	T centre II	T centre III
Zero-field saturation power (P_{sat})	0.08(1) μW ($t_{\text{exc}} = 800$ ns)	1.3(1) μW ($t_{\text{exc}} = 100$ ns)	-
At-field saturation power ($P_{\text{sat,B}}$)	-	2.5(2) μW ($t_{\text{exc}} = 100$ ns)	1.3(1) μW ($t_{\text{exc}} = 100$ ns)
Resonance frequency (P_{sat})	226.128,042(2) THz	226.130,610(1) THz	226.135,82(2) THz
Inhomo. linewidth (P_{sat})	1.703(6) GHz	3.8(1) GHz	3.9(1) GHz
Holeburning. linewidth (P_{sat})	323(2) MHz	880(50) MHz	-
Holeburning. linewidth (low power)	33(5) MHz	64(4) MHz	-
$g^{(2)}(0)$	0.26(2)	0.186(4)	0.372(9)
Cavity centre frequency	226.136(4) THz	226.135,12(6) THz	226.124(1) THz
Cavity Q factor	880(40)	1,743(2)	630(90)
Purcell enhanced lifetime	691(1) ns	602(9) ns	530(10) ns
Operating temperature	1.45–2.5 K	0.4 K	0.4 K
Pressure environment	20 mbar (Helium vapor)	10×10^{-6} mbar	10×10^{-6} mbar
Applied B -field	0	0 or 0.755 T	0.755 T
Hole g-factor, g_h	-	0.96(5)	1.26(5)

TABLE S1. Measured optical and cavity parameters for the three T centres investigated in this work. The inhomogeneous saturation power, P_{sat} is obtained from PLE spectra at zero-field. The at-field saturation power, $P_{\text{sat,B}}$ is obtained from PLE under equal excitation of both ground states (*e.g.* PLE while pumping the A and B transitions). The power is calibrated with a measurement before the circulator that connects to the fibre array going to the device. For T centre I we calibrate the power with an excitation pulse length of $t_{\text{exc}} = 800$ ns and for T centres II and III we measure saturation with $t_{\text{exc}} = 100$ ns which accounts for the difference in saturation power between the centres. We estimate 50% grating coupler efficiency, leading to the same reduction in final power at the T centre. The resonance frequency and the inhomogeneous and saturation holeburning linewidths were taken at the saturation power P_{sat} . The lowest measured saturation holeburning linewidths were taken at $P = 0.001(2) P_{\text{sat}}$ and $P = 0.007(2) P_{\text{sat}}$ for T centres I and II respectively. The zero-delay $g^{(2)}$ values indicate that these centres have emission primarily due to single centres and have been normalized to the long-time uncorrelated $g^{(2)}(\tau)$ rate. The cavity centre frequency and cavity Q factor were obtained by measuring reflection spectra. The applied field for the RC-PLE and the two-colour correlation measurements was 0 T. For the laser-induced excited-state mixing in TX_0 measurements, the applied field was 0.755 T.

Appendix SII: Off-resonant effects

In this section we explore the effects of off-resonant laser excitation in both the spectral diffusion and the TX_0 excited-state spin mixing phenomena.

1. Off-resonant excitation and spectral diffusion

We examine the role of off-resonant excitation by introducing a second laser at $f = 226.140,354$ THz, which pulses simultaneously with the resonant excitation laser at $f = 226.127,902$ THz during a $g^{(2)}(\tau)$ correlation measurement. A $g^{(2)}$ measurement is conceptually equivalent to the two-colour correlation measurements discussed in the main text when $\delta_2 - \delta_1 = 0$. There are two minor differences between $g^{(2)}$ and the two-colour correlation. First, $g^{(2)}$ measures correlations between every pulse, whereas the two-colour measurement only correlates alternating pulses with different detunings. Second, the two-colour correlation uses separate detectors for each spectral bin. This only affects the $\tau = 0$ bin, where photon antibunching suppresses coincidences. At nonzero delays, the effect is a constant scaling of the count rate, which we normalize out using the long-time data.

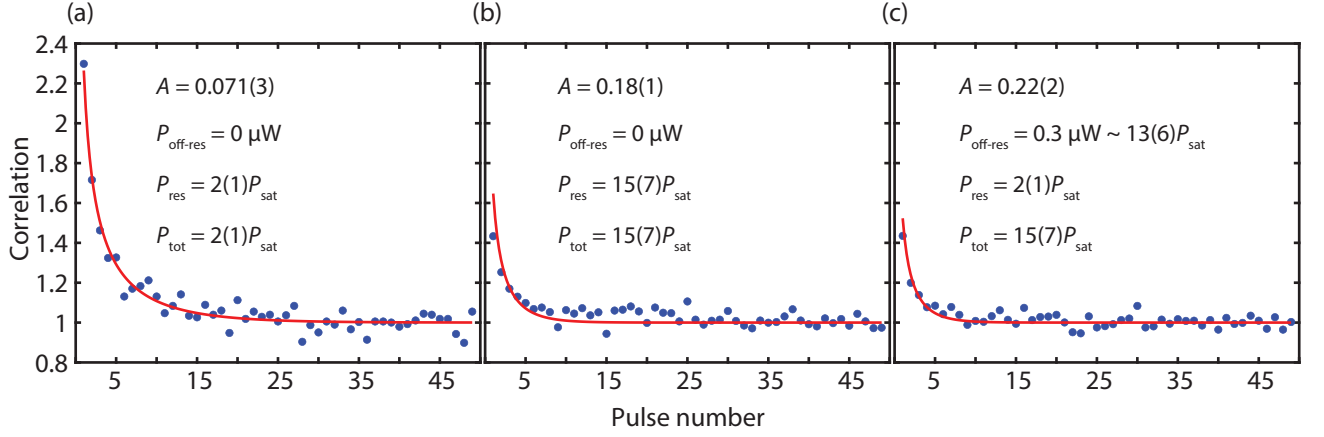


FIG. S1. The effect of off-resonant light on the spectral diffusion of a T centre. Markers are measured $g^{(2)}$ correlation (normalized to the long-time value) and the solid lines are one-parameter fits with the per-pulse SD rate, A as the free parameter. The value of β can be determined by the $g^{(2)}(0)$ value (not plotted). (a) A $g^{(2)}(\tau)$ measurement of T centre I with a resonant power of $P_{\text{res}} \approx 2P_{\text{sat}}$. (b) Same measurement with higher resonant excitation power of $P_{\text{res}} \approx 15P_{\text{sat}}$ showing a faster diffusion rate. (c) A measurement with the same resonant power as (a), but with an additional off-resonant laser $P_{\text{off-res}} \approx 13P_{\text{sat}}$, bringing the total power to $P_{\text{tot}} \approx 15P_{\text{sat}}$. The extracted spectral diffusion rate A in (c) closely matches that in (b), supporting the interpretation that laser-induced spectral diffusion is driven by the total excitation energy rather than by purely resonant processes.

Figure S1 presents a $g^{(2)}$ measurement on T centre I for three different power settings taken at a temperature of $T = 1.45$ K. We vary the resonant laser power between $P_{\text{res}} = 2(1)P_{\text{sat}}$ and $P_{\text{res}} = 15(1)P_{\text{sat}}$. To isolate the effect of off-resonant light, we perform a third measurement with $P_{\text{res}} = 2(1)P_{\text{sat}}$ and an additional off-resonant laser at $P_{\text{off-res}} = 13(6)P_{\text{sat}}$, yielding a total power equivalent to the higher-resonant-power case. We find that the mixing rate A under the off-resonant condition closely resembles that of the high-power resonant case, rather than the low-power case with equivalent resonant excitation. This observation supports the hypothesis that laser-induced SD arises from broadband excitation of a surrounding charge environment, rather than a purely resonant interaction with the emitter.

2. Off-resonant laser-induced excited state mixing

We probe whether the laser-induced excited state mixing results from resonant excitation or whether off-resonant excitation has a similar effect. We compare the populations measured after resonant excitation with the addition of a high-power, red-detuned laser ($f = 226.104,878$ THz) which pulses simultaneously with our resonant initialization lasers. The frequency is chosen to be within the cavity but far from any of the T centre optical transitions. On its own, this laser negligibly excites the emitter. By comparing the degree of spin mixing with and without simultaneous off-resonant light, we show that the mechanism driving the laser-induced spin mixing is not purely a resonant mechanism, but rather non-resonant light can also mix during the excitation pulse.

Figure S3 (b) summarizes our findings, showing the ratio of populations n_1/n_2 (as in the main text) for our two different excitation conditions. The calculated population ratio for the off-resonant experiment ($n_1/n_2 = 0.35(3)$) is higher than the ratio without off-resonant light ($n_1/n_2 = 0.13(3)$) but lower than the average of measurements at equivalent power for T centre II ($n_1/n_2 = 0.46(4)$). This discrepancy may be due to differences in the coupling to the cavity at different positions (leading to a slightly different effective power) or may indicate that the mixing rate displays some frequency dependence. In either case, these results rule out the hypothesis that the laser-induced mixing is the result of purely resonant effects.

Appendix SIII: Evidence for TX_0 spin state independence of laser mixing and tests on T Centre III

In this section, we demonstrate that the extracted post-pulse populations—and thus the degree of spin mixing—are independent of the initially prepared state. Verifying that n_1/n_2 is independent of the detection pathway helps establish that spin mixing is a fundamental effect of the excitation process, rather than a measurement artifact. It

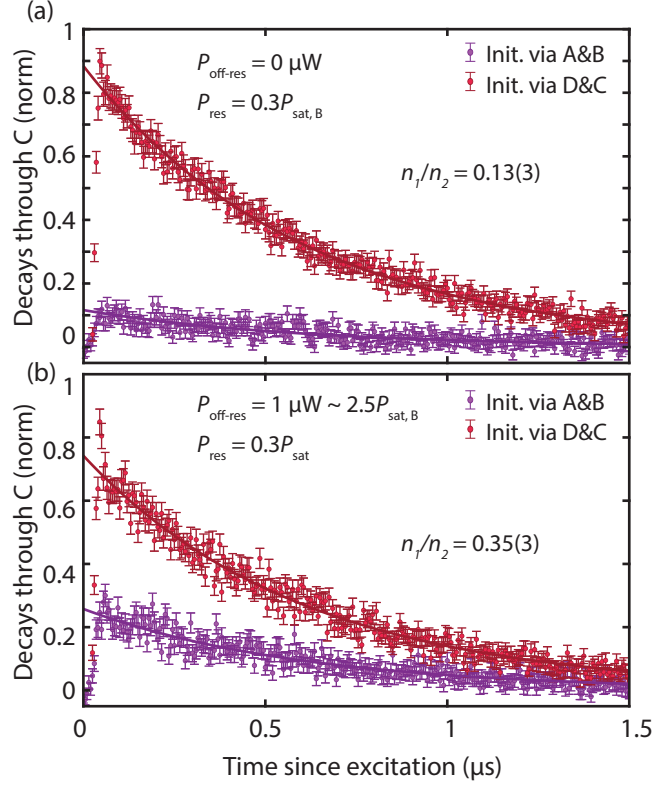


FIG. S2. The effect of off-resonant laser on the laser-induced excited state mixing. (a) Spin mixing measured at low resonant excitation power, $P = 0.3P_{\text{sat, B}}$, without off-resonant illumination. The extracted mixing fraction is $n_1/n_2 = 0.13(3)$. (b) Spin mixing under the same resonant conditions, but with the addition of an off-resonant laser at $P_{\text{off-res}} = 1 \mu\text{W}$, corresponding approximately to $2.5P_{\text{sat, B}}$. The mixing fraction increases to $n_1/n_2 = 0.35(3)$. We express the off-resonant power in units of $P_{\text{sat, B}}$ to facilitate direct comparison with the power levels used for resonant excitation in the main text, even though saturation is not strictly defined for off-resonant excitation. The observed increase in spin mixing with off-resonant power suggests that the mechanism driving excited-state spin transitions cannot be attributed solely to resonant optical excitation.

also supports that the ratio of populations under different initialization conditions serves as a reliable proxy for the relative populations of the two spin states under identical excitation. Specifically, we prepare the system in either $|h \uparrow\rangle$ or $|h \downarrow\rangle$ and measure post-pulse populations using filters aligned to both the C and B transitions, thereby probing both hole spin states.

Figure S3(a) shows the results for T centre II under all four combinations of initialization (either $|h \uparrow\rangle$ or $|h \downarrow\rangle$) and detection (via the C or B transition), at $P = 10.2P_{\text{sat, B}}$. The initial rise in signal is attributed to the collection path's acousto-optic modulator turning on. Here, n_1 (n_2) denotes the population in the detected state when the opposite (same) hole state is prepared. As expected, switching the detection filter to the B transition reverses the relative signal strengths for the two preparation states. Consequently, the ratio n_1/n_2 remains consistent regardless of whether we filter on the B or C transition. Figure S3 (b) plots n_1/n_2 versus excitation power for both filter configurations in T centre II, as well as for a separate device (T centre III) using the C transition. The agreement between the C and B data for T centre II confirms symmetric mixing between the hole states, validating n_1/n_2 as a reliable measure of mixing strength. The similar mixing behaviour observed in T centre III suggests that laser-induced spin mixing is not device-specific and may be a general characteristic of T centres under similar conditions.

Appendix SIV: Long dark time resonance check PLE

Here, we explore the linewidths of resonance-check photoluminescence excitation (RC-PLE) in the limit of long dark time, τ . We vary the dark time $\tau = 0, 1.5, 2.5, 3.0, \text{ms}$ for T centre II to investigate how spectral broadening evolves over extended intervals. We observe negligible broadening up to $\tau = 1.5 \text{ms}$, but find measurable linewidth increases at longer delays. Figure S4 shows the resonance-check PLE spectra as a function of detuning for each value

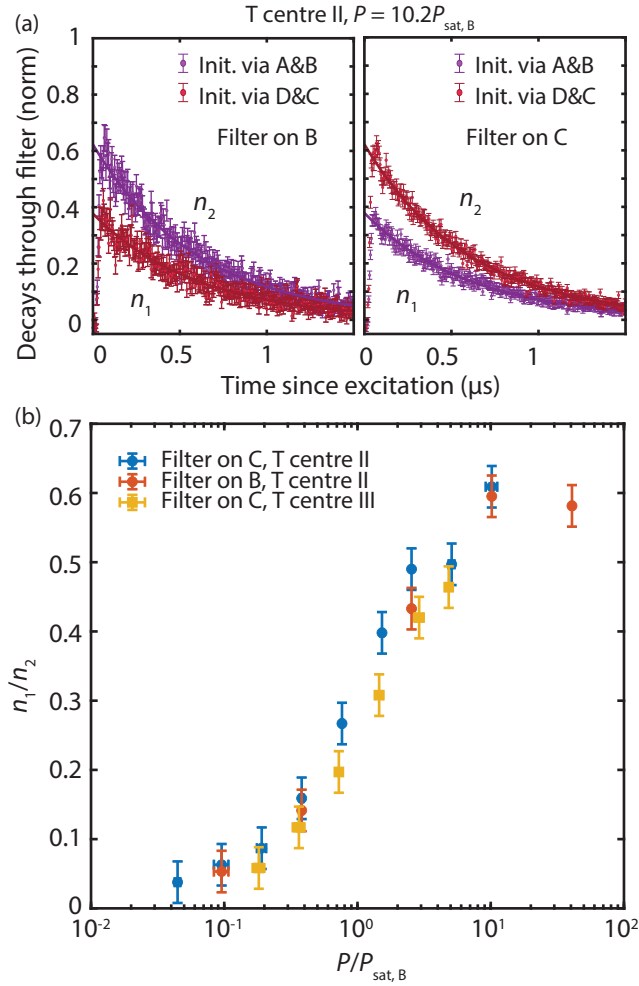


FIG. S3. (a) Comparison of laser-induced mixing observed when filtering emission through transitions B (left) and C (right) for T centre II. While populations associated with each initialization scheme swap when the filter is changed, the ratio of populations between prepared and unprepared states remains consistent, confirming symmetry in spin-state mixing rates. (b) Comparison of the population ratio n_1/n_2 for T centre II using filters on B and C, alongside measurements for another device (T centre III). All three data sets agree, indicating consistent mixing dynamics across multiple devices.

of τ . Counts are normalized to the number of probe pulses, corresponding to the probability of detecting a photon per probe pulse. For comparison, we also plot the unconditioned PLE spectrum, normalized in the same way. The ratio between the two spectra indicates the enhancement factor achieved through resonance-check preparation.

We fit Lorentzian functions to the resonance-check PLE spectra to determine the corresponding linewidths. No statistically significant broadening is observed for $\tau \leq 1.5$ ms; however, at longer dark times, a measurable increase in linewidth appears. This broadening is most pronounced on the high-frequency side of the spectra, suggesting asymmetry in the diffusion process. Figure S5 shows the extracted linewidth Γ as a function of the dark interval τ . The observed dependence of $\Gamma(\tau)$ deviates from the Ornstein–Uhlenbeck prediction: the second-derivative is positive, in contrast to the negative second-derivative expected for O-U dynamics. This suggests that a distinct physical mechanism may be responsible for the long-time spectral broadening.

Appendix SV: Temperature dependence of spectral diffusion

We increase the temperature of our device to $T = 2.5$ K and perform the same measurements at detuning values $\delta_2 - \delta_1 = \{0, 0.97, 1.9\}\sigma$. We jointly fit these correlation measurements using the same method as the main text. Figure S6 shows the two-colour correlation data at $T = 2.5$ K with an excitation power of $P = P_{\text{sat}}$. We find a value of $A = 0.025(1)$ that is somewhat lower than the value found at $T = 1.45$ K. We note that A cannot be meaningfully

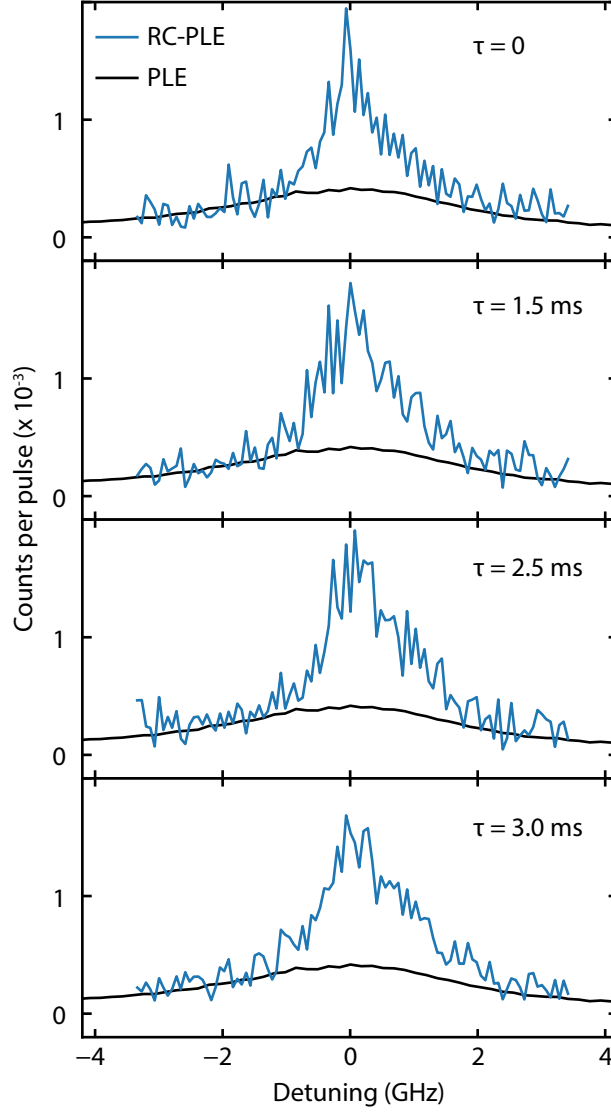


FIG. S4. RC-PLE linewidth broadening for T centre II as a function of dark time, τ . After detecting a ‘check pulse’, we introduce a variable delay before applying the ‘probe pulse’. For $\tau = 1.5$ ms, no statistically significant broadening is observed. However, for longer delays ($\tau \approx 2.5$ – 3.0 ms), we observe spectral broadening—on the order of 200–500 MHz—particularly on the high-frequency side of the spectrum. The RC-PLE data are normalized to the number of counts per probe pulse, representing the conditional probability of detection given a preceding check pulse. For the regular PLE, we plot the unconditional detection probability per shot. The ratio between these two traces indicates the enhancement achieved through the resonance-check scheme.

compared between these experiments due to reconfiguring the apparatus which may produce systematic variation in delivered power.

Appendix SVI: Ornstein-Uhlenbeck Model

In this section, we derive the Ornstein-Uhlenbeck model fitted to our spectral diffusion measurements from a microscopic discrete-charge model [56]. For related discussions, see Refs. [38, 57, 58]. We model our local environment as an ensemble of N charges, each equally coupled to the T centre, and each taking time-dependent values of ± 1 such that the i^{th} charge will be $c_i(t) \in \{-1, +1\}$ at time t . If each charge contributes a small perturbation to the transition frequency, then the centre frequency (up to an overall scaling factor) will be given by

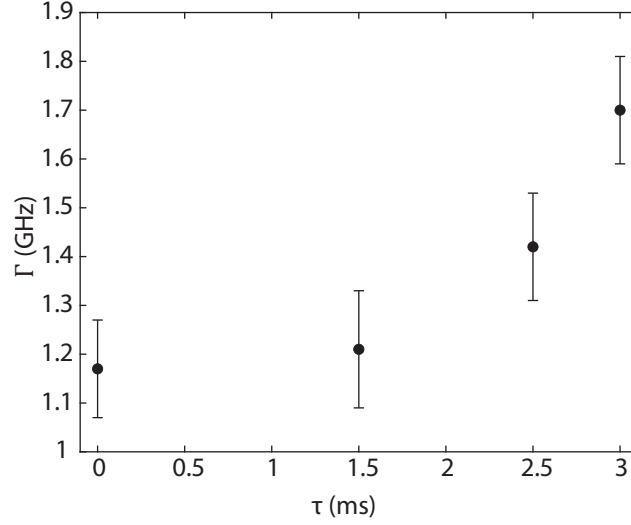


FIG. S5. Linewidths are extracted by fitting Lorentzians to the RC-PLE spectra shown in Fig. S4. The resulting linewidths, Γ , are plotted here as a function of the dark interval τ between the check and probe pulses. No statistically significant broadening is observed for $\tau = 1.5$ ms; however, for longer delays ($\tau \gtrsim 2.5$ ms), a gradual increase in linewidth is apparent.

$$\delta = \sum_{i=1}^N c_i / N. \quad (\text{S1})$$

At each time step, we scramble X charges—meaning each selected charge is randomly assigned a value of ± 1 . We introduce the variable $\alpha^* = \frac{X}{N}$ which is the fraction of charges in the ensemble that are scrambled each time step. We consider the limit of large N but finite α^* . The change in δ for each time step will be,

$$\mathbb{E}[\Delta\delta|\delta(t)] = -\alpha^*\delta(t). \quad (\text{S2})$$

As the overall sum of charges moves away from zero, the odds of flipping a charge that brings the distribution back to zero becomes higher. The variance per time step will be proportional to the number of charges scrambled, i.e., X . Therefore, the problem is mapped to a random walk with a restoring force,

$$\Delta\delta(t) = -\alpha^*\delta(t) + \sqrt{X}\xi_t, \quad (\text{S3})$$

where ξ_t is a Gaussian random variable with mean of 0 and standard deviation 1. We would like to find the correlations of the frequency as a function of time. We note the conceptual similarities to the problem of magnetization fluctuations in a paramagnet as a function of time.

Next we move to the continuous limit of this problem using

$$\frac{d\delta}{dt} = -\alpha\delta(t) + \sqrt{2D}\eta(t), \quad (\text{S4})$$

where $\eta(t) = \frac{dW}{dt}$ is a white noise term (derivative of the Wiener process, $W(t)$), α is the spectral diffusion rate and D is a diffusion constant.

The conditional probability that the centre frequency takes the value $\delta(t) = \delta_2$ at time t , given $\delta(0) = \delta_1$, is given by

$$P(\delta_1, t | \delta_0, 0) = \frac{1}{\sqrt{2\pi(1 - e^{-2\alpha t})}} \exp \left[-\frac{(\delta_2 - \delta_1 e^{-\alpha t})^2}{2(1 - e^{-2\alpha t})} \right], \quad (\text{S5})$$

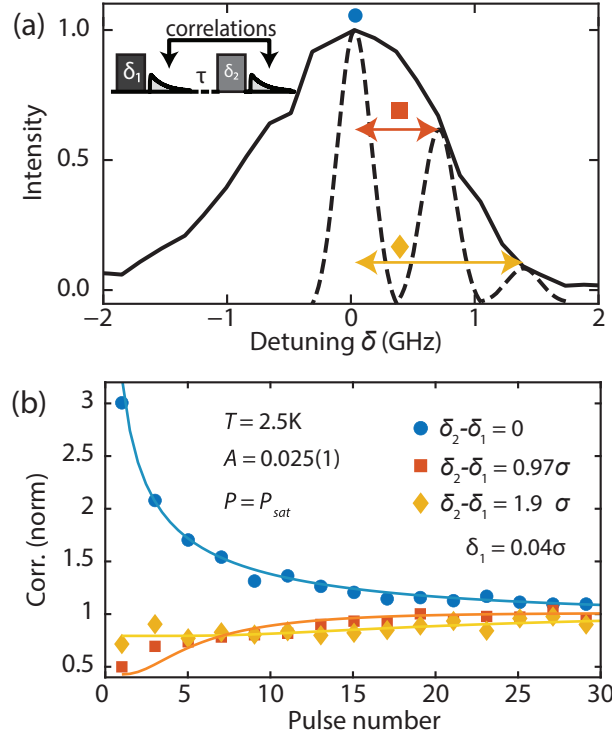


FIG. S6. (a) Laser detunings from the centre of the inhomogeneous line (solid) and modelled homogeneous lines at P_{sat} (dashed) (b) Two-colour correlation data for $T = 2.5\text{K}$ normalized to the long-time value. Solid lines are fits to the O-U model described in the main text where A is the sole fitting parameter. The fitted α is larger than that which was found at $T = 2.5\text{K}$. This difference may result from a systematic change in delivered excitation power, introduced during fibre realignment required for temperature switching.

where we have made the rescaling $D = \alpha$ for convenience (equivalent to rescaling $\delta(t)$ in units of the inhomogeneous or long-time standard deviation). Figure S7 displays $P(\delta_2, t | \delta_1, 0)$ as a function of time for $\delta_1 = 2\sigma$. Over time, the narrow peak initially centred near 2σ broadens, shifts and converges to the inhomogeneous distribution.

To model the correlation data, we include a finite dark count term, β , and normalize the correlation such that $C \rightarrow 1$ at long times yielding

$$C = \beta + \sqrt{2\pi} e^{\delta_2^2/2} [1 - \beta] P(\delta_2, t | \delta_1, 0). \quad (\text{S6})$$

We define a per-pulse mixing rate by integrating over the duration of the excitation pulse:

$$A = \int_{\text{pulse}} \alpha dt = \alpha t_{\text{pulse}}, \quad (\text{S7})$$

where t_{pulse} is the excitation pulse duration. We can interpret A as the fraction of the local charge environment that is reconfigured during each pulse.

We determine β from three sources of background contributions to the correlation signal. These include: $P(\delta_2|\text{noise})$ (true second-bin signal with a first-bin non-signal [noise] count), $P(\text{noise}|\delta_1)$, and $P(\text{noise}|\text{noise})$. We measure the background subtracted uncorrelated count rates corresponding to the different spectral positions. Let R_1 and R_2 denote the T centre count rates at $f = \delta_1$ and $f = \delta_2$, respectively, and let R_N denote the noise count rate. The resulting expression for β is:

$$\beta = \frac{R_N(R_N + R_1 + R_2)}{R_N(R_N + R_1 + R_2) + R_1 R_2}, \quad (\text{S8})$$

which we compute from our measured PLE spectrum.

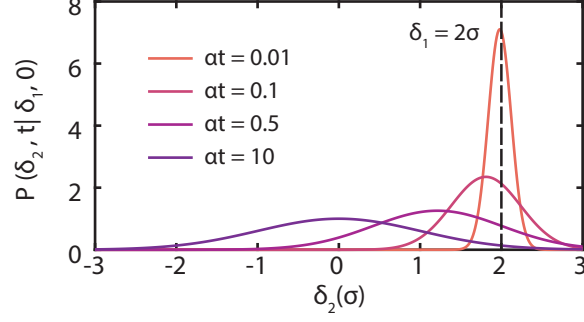


FIG. S7. Plot of Eq. (S5) showing the conditional probability amplitude distribution for an initial detuning $\delta_1 = 2\sigma$. The probability amplitudes have been normalized to the maximum of the long-time inhomogeneous distribution. At early times ($at \ll 1$) the distribution remains localized near the initial frequency δ_1 . As time evolves the distribution broadens toward the steady-state inhomogeneous distribution with mean $\delta_2 = 0$.

Appendix SVII: Resonance check for multi-emitter entanglement

In this section, we analyze the statistics of a resonance check in the context of multi-qubit preparation. We consider N qubits, each with independent excitation and photon detection probabilities. The probability of detecting a photon on any given pulse is

$$\eta_{SD}\eta_{\text{det}} = \frac{1}{M}, \quad (\text{S1})$$

where η_{SD} is the ratio of the homogeneous to inhomogeneous linewidths, and η_{det} is the detection efficiency. For simplicity, we assume coherent excitation by an optical π -pulse with unit excitation efficiency, $\eta_{\text{exc}} = 1$. For non-ideal excitation efficiency, η_{exc} enters the analysis in the same way as η_{det} , effectively rescaling the detection probability.

We analyze the use of charge resonance checks across all qubits in parallel, continuing until each qubit is spectrally prepared. In this setting, the total preparation time is limited by the slowest qubit in the ensemble. We consider regimes in which a charge resonance check will result in overall sequence speedup.

Let X_i denote the number of attempts required to observe a photon detection in the check-probe sequence for the i^{th} qubit. Then, X_i is a geometric random variable with mean $\mathbb{E}[X_i] = M$, a probability density function (PDF) of

$$\Pr(X_i = k) = \left(1 - \frac{1}{M}\right)^{k-1} \frac{1}{M}, \quad (\text{S2})$$

and a cumulative density function (CDF) of

$$\Pr(X_i \leq k) = 1 - \left(1 - \frac{1}{M}\right)^k. \quad (\text{S3})$$

For N qubits, the total number of attempts required to spectrally prepare all qubits is given by

$$T = \max\{X_1, X_2, \dots\}. \quad (\text{S4})$$

We now compute the expected value of T using the tail-sum formula:

$$\mathbb{E}[T] = \sum_{k=1}^{\infty} \Pr(T \geq k) = \sum_{k=1}^{\infty} [1 - \Pr(T < k)] = \sum_{k=1}^{\infty} \left[1 - \prod_{i=1}^N \Pr(X_i \leq k-1)\right]. \quad (\text{S5})$$

The expression in the product is the CDF for our geometric random variable and hence,

$$\mathbb{E}[T] = \sum_{k=1}^{\infty} \left[1 - \left\{ 1 - \left(1 - \frac{1}{M} \right)^{k-1} \right\}^N \right], \quad (\text{S6})$$

which has a closed form representation

$$\mathbb{E}[T] = \sum_{j=1}^N (-1)^{j+1} \binom{N}{j} \frac{1}{1 - (1 - 1/M)^j}. \quad (\text{S7})$$

We next compare two approaches for spectrally preparing N qubits: parallel preparation with resonance checks versus repeated unconditioned attempts. Let η_{SD}^* denote the ratio of the homogeneous to check-probe linewidth, and let τ be the duration of a single excitation-check attempt. In the first scheme, all N qubits are excited simultaneously, and their photon outputs are independently checked for spectral alignment. The average amount of time required to successfully generate these photons will be

$$\text{Time (independent check)} = \tau \left(\frac{1}{\eta_{\text{SD}} \eta_{\text{Det}}} \right)^N. \quad (\text{S8})$$

For the resonance-checked approach, the average preparation time is

$$\text{Time (resonance check)} = \tau (1 + \mathbb{E}[T]) \left(\frac{1}{\eta_{\text{SD}}^* \eta_{\text{Det}}} \right)^N. \quad (\text{S9})$$

The resulting speedup is

$$\text{Speedup} = \left(\frac{\eta_{\text{SD}}^*}{\eta_{\text{SD}}} \right)^N / (1 + \mathbb{E}[T]). \quad (\text{S10})$$

Note that $\mathbb{E}[T]$ scales as $\log N$, whereas the numerator grows exponentially with N . Thus, the expected speedup always exceeds 1 for sufficiently large N .

-
- [1] G. Wolfowicz, F. J. Heremans, C. P. Anderson, S. Kanai, H. Seo, A. Gali, G. Galli, and D. D. Awschalom, Quantum guidelines for solid-state spin defects, *Nature Reviews Materials* **6**, 906 (2021).
 - [2] C. P. Michaels, J. A. Martinez, R. Debroux, R. A. Parker, A. M. Stramma, L. I. Huber, C. M. Purser, M. Atature, and D. A. Gangloff, Multidimensional cluster states using a single spin-photon interface coupled strongly to an intrinsic nuclear register, *Quantum* **5**, 565 (2021).
 - [3] P. J. Stas, Y. Q. Huan, B. Machielse, E. N. Knall, A. Suleymanzade, B. Pingault, M. Sutula, S. W. Ding, C. M. Knaut, D. R. Assumpcao, Y. C. Wei, M. K. Bhaskar, R. Riedinger, D. D. Sukachev, H. Park, M. Lončar, D. S. Levonian, and M. D. Lukin, Robust multi-qubit quantum network node with integrated error detection, *Science* **378**, 557 (2022).
 - [4] C. M. Knaut, A. Suleymanzade, Y.-C. Wei, D. R. Assumpcao, P.-J. Stas, Y. Q. Huan, B. Machielse, E. N. Knall, M. Sutula, G. Baranes, N. Sinclair, C. De-Eknamkul, D. S. Levonian, M. K. Bhaskar, H. Park, M. Lončar, and M. D. Lukin, Entanglement of nanophotonic quantum memory nodes in a telecom network, *Nature* **629**, 573 (2024).
 - [5] S. Simmons, Scalable fault-tolerant quantum technologies with silicon color centers, *PRX Quantum* **5**, 010102 (2024).
 - [6] Y.-C. Wei, P.-J. Stas, A. Suleymanzade, G. Baranes, F. Machado, Y. Q. Huan, C. M. Knaut, W. S. Ding, M. Merz, E. N. Knall, U. Yazlar, M. Sirotn, I. W. Wang, B. Machielse, S. F. Yelin, J. Borregaard, H. Park, M. Loncar, and M. D. Lukin, Universal distributed blind quantum computing with solid-state qubits, (2024).
 - [7] G. de Glinasty, P. Hilaire, P. E. Emeriau, S. C. Wein, A. Salavrakos, and S. Mansfield, A Spin-Optical Quantum Computing Architecture, *Quantum* **8**, 1423 (2024).
 - [8] A. Gritsch, A. Ulanowski, and A. Reiserer, Purcell enhancement of single-photon emitters in silicon, *Optica* **10**, 783 (2023).
 - [9] B. Merkel, A. Ulanowski, and A. Reiserer, Coherent and Purcell-Enhanced Emission from Erbium Dopants in a Cryogenic High-Q Resonator, *Physical Review X* **10**, 041025 (2020).
 - [10] C. Li, P. Guo, S. W. Xie, L. W. Luo, S. Y. Siew, X. Luo, B. Dong, H. Y. Zheng, W. Zhang, F. Gao, G.-Q. Lo, A. Song, and B. Li, Review of Silicon Photonics Technology and Platform Development, *Journal of Lightwave Technology*, Vol. 39, Issue 13, pp. 4374-4389 **39**, 4374 (2021).

- [11] J. Wolters, N. Sadzak, A. W. Schell, T. Schröder, and O. Benson, Measurement of the ultrafast spectral diffusion of the optical transition of nitrogen vacancy centers in nano-size diamond using correlation interferometry, *Phys. Rev. Lett.* **110**, 027401 (2013).
- [12] J. Heiler, J. Körber, E. Hesselmeier, P. Kuna, R. Stöhr, P. Fuchs, M. Ghezellou, J. Ul-Hassan, W. Knolle, C. Becher, F. Kaiser, and J. Wrachtrup, Spectral stability of v2 centres in sub-micron 4h-sic membranes, *npj Quantum Materials* **9**, 34 (2024).
- [13] D. B. Higginbottom, A. T. K. Kurkjian, C. Chartrand, M. Kazemi, N. A. Brunelle, E. R. MacQuarrie, J. R. Klein, N. R. Lee-Hone, J. Stacho, M. Ruether, C. Bowness, L. Bergeron, A. DeAbreu, S. R. Harrigan, J. Kanaganayagam, D. W. Marsden, T. S. Richards, L. A. Stott, S. Roorda, K. J. Morse, M. L. W. Thewalt, and S. Simmons, Optical observation of single spins in silicon, *Nature* **607**, 266 (2022).
- [14] A. Johnston, U. Felix-Rendon, Y.-E. Wong, and S. Chen, Cavity-coupled telecom atomic source in silicon, *Nature Communications* **15**, 2350 (2024).
- [15] B. Lefaucher, Y. Baron, J.-B. Jager, V. Calvo, C. Elsässer, G. Coppola, F. Mazen, S. Kerdilès, F. Cache, A. Dréau, J.-M. Gérard, and à. Grenoble, Bright single-photon source in a silicon chip by nanoscale positioning of a color center in a microcavity, (2025).
- [16] W. Redjem, Y. Zhiyenbayev, W. Qarony, V. Ivanov, C. Papapanos, W. Liu, K. Jhuria, Z. Y. Al Balushi, S. Dhuey, A. Schwartzberg, L. Z. Tan, T. Schenkel, and B. Kanté, All-silicon quantum light source by embedding an atomic emissive center in a nanophotonic cavity, *Nature Communications* 2023 14:1 **14**, 1 (2023).
- [17] V. Saggio, C. Errando-Herranz, S. Gyger, C. Panuski, M. Prabhu, L. De Santis, I. Christen, D. Ornelas-Huerta, H. Raniwala, C. Gerlach, M. Colangelo, and D. Englund, Cavity-enhanced single artificial atoms in silicon, *Nature Communications* 2024 15:1 **15**, 1 (2024).
- [18] L. Komza, X. Zhang, H. Song, Y.-L. Tang, X. Wei, and A. Sipahigil, Multiplexed color centers in a silicon photonic cavity array (2025), arXiv:2501.17339.
- [19] F. Afzal, M. Akhlaghi, S. J. Beale, O. Bedroya, K. Bell, L. Bergeron, K. Bonsma-Fisher, P. Bychkova, Z. M. E. Chaisson, C. Chartrand, C. Clear, A. Darcie, A. DeAbreu, C. DeLisle, L. A. Duncan, C. D. Smith, J. Dunn, A. Ebrahimi, N. Evetts, D. F. Pinheiro, P. Fuentes, T. Georgiou, B. Guha, R. Haenel, D. Higginbottom, D. M. Jackson, N. Jahed, A. Khorshidahmad, P. K. Shandilya, A. T. K. Kurkjian, N. Lauk, N. R. Lee-Hone, E. Lin, R. Litynsky, D. Lock, L. Ma, I. MacGilp, E. R. MacQuarrie, A. Mar, A. M. Khah, A. Matias, E. Meyer-Scott, C. P. Michaels, J. Motira, N. K. Noori, E. Ospadov, E. Patel, A. Patscheider, D. Paulson, A. Petruk, A. L. Ravindranath, B. Reznichenko, M. Ruether, J. Ruscica, K. Saxena, Z. Schaller, A. Seidlitz, J. Senger, Y. S. Lee, O. Sevoyan, S. Simmons, O. Soykal, L. Stott, Q. Tran, S. Tserkis, A. Ulhaq, W. Vine, R. Weeks, G. Wolfowicz, and I. Yoneda, Distributed Quantum Computing in Silicon, arXiv 2406.01704 (2024).
- [20] K. Saeedi, S. Simmons, J. Z. Salvail, P. Dluhy, H. Riemann, N. V. Abrosimov, P. Becker, H.-J. Pohl, J. J. L. Morton, and M. L. W. Thewalt, Room-temperature quantum bit storage exceeding 39 minutes using ionized donors in silicon-28, *Science* **342**, 830 (2013).
- [21] C. Chartrand, L. Bergeron, K. J. Morse, H. Riemann, N. V. Abrosimov, P. Becker, H.-J. Pohl, S. Simmons, and M. L. W. Thewalt, Highly enriched ^{28}Si reveals remarkable optical linewidths and fine structure for well-known damage centers, *Phys. Rev. B* **98**, 195201 (2018).
- [22] L. Bergeron, C. Chartrand, A. T. K. Kurkjian, K. J. Morse, H. Riemann, N. V. Abrosimov, P. Becker, H.-J. Pohl, M. L. W. Thewalt, and S. Simmons, Silicon-Integrated Telecommunications Photon-Spin Interface, *PRX Quantum* **1**, 20301 (2020).
- [23] A. DeAbreu, C. Bowness, A. Alizadeh, C. Chartrand, N. A. Brunelle, E. R. MacQuarrie, N. R. Lee-Hone, M. Ruether, M. Kazemi, A. T. K. Kurkjian, S. Roorda, N. V. Abrosimov, H.-J. Pohl, M. L. W. Thewalt, D. B. Higginbottom, and S. Simmons, Waveguide-integrated silicon t centres, *Opt. Express* **31**, 15045 (2023).
- [24] S. D. Barrett and P. Kok, Efficient high-fidelity quantum computation using matter qubits and linear optics, *Physical Review A* **71**, 060310 (2005).
- [25] C. Cabrillo, J. Cirac, P. García-Fernández, and P. Zoller, Creation of entangled states of distant atoms by interference, *Physical Review A* **59**, 1025 (1999).
- [26] J. M. Brevoord, L. De Santis, T. Yamamoto, M. Pasini, N. Codreanu, T. Turan, H. K. Beukers, C. Waas, and R. Hanson, Heralded initialization of charge state and optical-transition frequency of diamond tin-vacancy centers, *Phys. Rev. Appl.* **21**, 054047 (2024).
- [27] S. L. Hermans, M. Pompili, L. D. Santos Martins, A. R-P Montblanch, H. K. Beukers, S. Baier, J. Borregaard, and R. Hanson, Entangling remote qubits using the single-photon protocol: an in-depth theoretical and experimental study, *New Journal of Physics* **25**, 013011 (2023).
- [28] E. R. Schmidgall, S. Chakravarthi, M. Gould, I. R. Christen, K. Hestroffer, F. Hatami, and K.-M. C. Fu, Frequency control of single quantum emitters in integrated photonic circuits, *Nano Letters* **18**, 1175 (2018).
- [29] V. M. Acosta, C. Santori, A. Faraon, Z. Huang, K.-M. C. Fu, A. Stacey, D. A. Simpson, K. Ganesan, S. Tomljenovic-Hanic, A. D. Greentree, S. Praver, and R. G. Beausoleil, Dynamic stabilization of the optical resonances of single nitrogen-vacancy centers in diamond, *Phys. Rev. Lett.* **108**, 206401 (2012).
- [30] M. Pompili, S. L. Hermans, S. Baier, H. K. Beukers, P. C. Humphreys, R. N. Schouten, R. F. Vermeulen, M. J. Tiggeleman, L. dos Santos Martins, B. Dirkse, S. Wehner, and R. Hanson, Realization of a multinode quantum network of remote solid-state qubits, *Science* **372**, 259 (2021).
- [31] G. Sallen, A. Tribu, T. Aichele, R. André, L. Besombes, C. Bougerol, M. Richard, S. Tatarenko, K. Kheng, and J.-P. Poizat, Subnanosecond spectral diffusion measurement using photon correlation, *Nature Photonics* **4**, 696 (2010).
- [32] C. M. Lee, F. Islam, S. Harper, M. A. Buyukaya, D. Higginbottom, S. Simmons, and E. Waks, High-Efficiency Single Photon Emission from a Silicon T-Center in a Nanobeam, *ACS Photonics* **10**, 3844 (2023).

- [33] F. Islam, C.-M. Lee, S. Harper, M. H. Rahaman, Y. Zhao, N. K. Vij, and E. Waks, Cavity enhanced emission from a silicon T center, *Nano Letters* 10.1021/acs.nanolett.3c04056 (2023).
- [34] M. Dobinson, C. Bowness, S. A. Meynell, C. Chartrand, E. Hoffmann, M. Gascoine, I. MacGilp, F. Afzal, C. Dangel, N. Jahed, M. L. W. Thewalt, S. Simmons, and D. B. Higginbottom, Electrically-triggered spin-photon devices in silicon (2025), arXiv:2501.10597 [quant-ph].
- [35] A. M. Day, C. Zhang, C. Jin, H. Song, M. Sutula, A. Sipahigil, M. K. Bhaskar, and E. L. Hu, Probing negative differential resistance in silicon with a p-i-n diode-integrated t center ensemble (2025), arXiv:2501.11888.
- [36] E. R. MacQuarrie, C. Chartrand, D. B. Higginbottom, K. J. Morse, V. A. Karasyuk, S. Roorda, and S. Simmons, Generating t centres in photonic silicon-on-insulator material by ion implantation, *New Journal of Physics* **23**, 103008 (2021).
- [37] See Supplemental Material at [URL will be inserted by publisher] for: a summary of T centre device properties; off-resonant effects; evidence of spin-state symmetry in laser-induced mixing; laser-induced mixing on another device; dark time resonance check PLE; spectral diffusion at a second temperature point; a discussion of the Ornstein Uhlenbeck spectral diffusion model; analysis of the charge resonance check efficiency.
- [38] A. Delteil, S. Buil, and J.-P. Hermier, Photon statistics of resonantly driven spectrally diffusive quantum emitters, *Phys. Rev. B* **109**, 155308 (2024).
- [39] G. L. van de Stolpe, L. J. Feije, S. J. H. Loenen, A. Das, G. M. Timmer, T. W. de Jong, and T. H. Taminiau, Check-probe spectroscopy of lifetime-limited emitters in bulk-grown silicon carbide, *npj Quantum Information* **11**, 31 (2025).
- [40] J. Görlitz, D. Herrmann, P. Fuchs, T. Iwasaki, T. Taniguchi, D. Rogalla, D. Hardeman, P.-O. Colard, M. Markham, M. Hatano, and C. Becher, Coherence of a charge stabilised tin-vacancy spin in diamond, *npj Quantum Information* **8**, 45 (2022).
- [41] K. Azuma, K. Tamaki, and H.-K. Lo, All-photonic quantum repeaters, *Nature Communications* **6**, 6787 (2015).
- [42] P. Hilaire, E. Barnes, S. E. Economou, and F. Grosshans, Error-correcting entanglement swapping using a practical logical photon encoding, *Phys. Rev. A* **104**, 052623 (2021).
- [43] R. Zhang, L.-Z. Liu, Z.-D. Li, Y.-Y. Fei, X.-F. Yin, L. Li, N.-L. Liu, Y. Mao, Y.-A. Chen, and J.-W. Pan, Loss-tolerant all-photonic quantum repeater with generalized shor code, *Optica* **9**, 152 (2022).
- [44] S. C. Wein, T. G. de Brugiñre, L. Music, P. Senellart, B. Bourdoncle, and S. Mansfield, Minimizing resource overhead in fusion-based quantum computation using hybrid spin-photon devices (2024), arXiv:2412.08611.
- [45] J. Borregaard, H. Pichler, T. Schröder, M. D. Lukin, P. Lodahl, and A. S. Sørensen, One-way quantum repeater based on near-deterministic photon-emitter interfaces, *Phys. Rev. X* **10**, 021071 (2020).
- [46] C. Clear, S. Hosseini, A. AlizadehKhaledi, N. Brunelle, A. Woolverton, J. Kanaganayagam, M. Kazemi, C. Chartrand, M. Keshavarz, Y. Xiong, L. Alaerts, O. O. Soykal, G. Hautier, V. Karassiouk, M. Thewalt, D. Higginbottom, and S. Simmons, Optical-transition parameters of the silicon t center, *Phys. Rev. Appl.* **22**, 064014 (2024).
- [47] X. Zhang, N. Fiaschi, L. Komza, H. Song, T. Schenkel, and A. Sipahigil, Laser-induced spectral diffusion of T centers in silicon nanophotonic devices (2025), Manuscript in preparation.
- [48] S. Taherizadegan, F. K. Asadi, J.-W. Ji, D. Higginbottom, and C. Simon, Exploring the feasibility of probabilistic and deterministic quantum gates between T-centers in silicon (2025), manuscript in preparation.
- [49] H. D. Robinson and B. B. Goldberg, Light-induced spectral diffusion in single self-assembled quantum dots, *Phys. Rev. B* **61**, R5086 (2000).
- [50] M. Holmes, S. Kako, K. Choi, M. Arita, and Y. Arakawa, Spectral diffusion and its influence on the emission linewidths of site-controlled gan nanowire quantum dots, *Phys. Rev. B* **92**, 115447 (2015).
- [51] K. é. Gao, I. Solovev, M. Holmes, M. æ. Arita, and Y. è. Arakawa, Nanosecond-scale spectral diffusion in the single photon emission of a gan quantum dot, *AIP Advances* **7**, 125216 (2017).
- [52] N. Ha, T. Mano, Y.-L. Chou, Y.-N. Wu, S.-J. Cheng, J. Bocquel, P. M. Koenraad, A. Ohtake, Y. Sakuma, K. Sakoda, and T. Kuroda, Size-dependent line broadening in the emission spectra of single gaas quantum dots: Impact of surface charge on spectral diffusion, *Phys. Rev. B* **92**, 075306 (2015).
- [53] S. Manna, H. Huang, S. F. C. da Silva, C. Schimpf, M. B. Rota, B. Lehner, M. Reindl, R. Trotta, and A. Rastelli, Surface passivation and oxide encapsulation to improve optical properties of a single gaas quantum dot close to the surface, *Applied Surface Science* **532**, 147360 (2020).
- [54] Y. Xiong, J. Zheng, S. McBride, X. Zhang, S. M. Griffin, and G. Hautier, Discovery of T center-like quantum defects in silicon, *Journal of the American Chemical Society* **146**, 30046 (2024).
- [55] Q. Quan and M. Loncar, Deterministic design of wavelength scale, ultra-high q photonic crystal nanobeam cavities, *Opt. Express* **19**, 18529 (2011).
- [56] G. E. Uhlenbeck and L. S. Ornstein, On the theory of the brownian motion, *Phys. Rev.* **36**, 823 (1930).
- [57] C. W. Gardiner, *Handbook of stochastic methods for physics, chemistry and the natural sciences*, 3rd ed., Springer Series in Synergetics, Vol. 13 (Springer-Verlag, Berlin, 2004) pp. xviii+415.
- [58] N. V. Kampen, Chapter iii - stochastic processes, in *Stochastic Processes in Physics and Chemistry (Third Edition)*, North-Holland Personal Library, edited by N. V. Kampen (Elsevier, Amsterdam, 2007) third edition ed., pp. 52–72.